

# Surface band characters of Weyl semimetal candidate material $\text{MoTe}_2$ revealed by one-step ARPES theory

Ryota Ono,<sup>1</sup> Alberto Marmodoro,<sup>2</sup> Jakub Schusser,<sup>3</sup> Yositaka Nakata,<sup>1</sup> Eike F. Schwier,<sup>4,\*</sup> Jürgen Braun,<sup>5</sup> Hubert Ebert,<sup>5</sup> Ján Minár,<sup>3</sup> Kazuyuki Sakamoto,<sup>6,7</sup> and Peter Krüger<sup>8,†</sup>

<sup>1</sup>*Graduate School of Science and Engineering, Chiba University, Inage-ku, Chiba-shi 265-8522, Japan*

<sup>2</sup>*FZU - Institute of Physics od the Czech Academy of Sciences,  
Cukrovarnicka 10, CZ-162 53 Prague, Czech Republic*

<sup>3</sup>*New Technologies - Research Center, University of West Bohemia, Univerzitní 8, 306 14 Plzeň, Czech Republic*

<sup>4</sup>*Hiroshima Synchrotron Radiation Center, Hiroshima University,  
Kagamiyama 2-313, Higashi-Hiroshima 739-0046, Japan*

<sup>5</sup>*Department of Chemistry, Ludwig Maximilians University München, Butenandtstraße 11, 81377 München, Germany*

<sup>6</sup>*Graduate School of Engineering and Molecular Chirality Research Center, Chiba University, Chiba 263-8522, Japan*

<sup>7</sup>*Department of Applied Physics, Osaka University, Osaka 565-0871, Japan*

<sup>8</sup>*Graduate School of Engineering and Molecular Chirality Research Center, Chiba University, Chiba 263-8522 Japan*

(Dated: May 25, 2022)

The layered 2D-material  $\text{MoTe}_2$  in the  $T_d$  crystal phase is a semimetal which has theoretically been predicted to possess topologically non-trivial bands corresponding to Weyl fermions. Clear experimental evidence by angle-resolved photoemission spectroscopy (ARPES) is, however, lacking, which calls for a careful examination of the relation between ground state band structure calculations and ARPES intensity plots. Here we report a study of the near Fermi-energy band structure of  $\text{MoTe}_2(T_d)$  by means of ARPES measurements, density functional theory, and one-step-model ARPES calculations. Good agreement between theory and experiment is obtained. We analyze the orbital character of the surface bands and its relation to the ARPES polarization dependence. We find that light polarization has a major effect on which bands can be observed by ARPES. For  $s$ -polarized light, the ARPES intensity is dominated by subsurface Mo  $d$  orbitals, while  $p$ -polarized light reveals the bands composed mainly derived from Te  $p$  orbitals. Suitable light polarization for observing either electron or hole pocket are determined.

---

\* Present address: Experimentelle Physik VII, Universität Würzburg, Am Hubland, D-97074 Würzburg, Germany

† [pkruger@chiba-u.jp](mailto:pkruger@chiba-u.jp)

## I. INTRODUCTION

Topological Weyl semimetals (WSMs) are receiving much attention because the quasiparticles at particular points in the band structure are a realization of mass-less Dirac fermions, so-called Weyl fermions [1]. WSMs have peculiar transport properties [2–5], including the quantum anomalous Hall effect, and the violation of separate number conservation laws for the left handed and right handed Weyl fermion in the presence of parallel electric and magnetic fields, known as chiral anomaly [6]. In a semi-metal, both the conduction and the valence bands cross the Fermi energy. In a WSM, there are special crossing points, called Weyl points, which correspond to topologically protected states. Weyl points come in pairs with opposite chirality. They are the end-points of the Fermi arc, i.e. the open Fermi line of the surface band structure. TaAs and related compounds, were the first materials in which WSM property was experimentally observed [1, 7–9]. More recently, another possible realization of WSMs was found in transition metal dichalcogenides (TMDC), e.g. WTe<sub>2</sub> [10–13]. TMDC are 2D-layered materials and particularly promising for electronic applications. TaAs and WTe<sub>2</sub> are classified as type-I and type-II WSMs, respectively [10]. Both types have point-like crossings at the Fermi energy, but in type-II WSM the cone-shaped bands are tilted in  $k$ -space. Also, type-I WSM respects Lorentz invariance, whereas type-II breaks it [10].

The TMDC molybdenum tellurite, in the low temperature MoTe<sub>2</sub>(T<sub>d</sub>) phase, has been proposed as a possible WSM material [14–17]. At room temperature, MoTe<sub>2</sub> crystallizes in the monoclinic, centrosymmetric 1T' phase. Upon cooling below 240 K MoTe<sub>2</sub> changes to the orthorhombic, non-centrosymmetric T<sub>d</sub> phase (space group  $Pmn2_1$ , No. 31) [18–21]. While the atomic structures of the 1T' and T<sub>d</sub> phases are similar, the fact that the T<sub>d</sub>-phase lacks inversion symmetry makes it a possible realization of type-II WSM, as proposed both on theoretical and experimental grounds [10, 14–17]. The surface band structure of MoTe<sub>2</sub>(T<sub>d</sub>) has been studied using ARPES by several authors [15–17] but the interpretation of the data is difficult without dedicated ARPES simulations including final state and matrix element effects. ARPES peak positions are routinely used for band mapping, but the peak intensities, which contain useful information about the electronic wave functions [22], is often left unexploited. The ARPES intensity and its light polarization dependence is determined not only by the initial state band character, but also by final state effects, in particular in spin-orbit coupled systems [23] such as WSMs. As a consequence, reliable ARPES calculations within the one-step model of photoemission are necessary for a correct interpretation of the experimental data. To the best of our knowledge, such calculations have not been reported yet.

Most ARPES studies of MoTe<sub>2</sub>(T<sub>d</sub>) have focused on the search for topologically non-trivial Weyl points and Fermi arcs [14–17]. While density functional theory (DFT) calculations have consistently found these features in the MoTe<sub>2</sub> surface band structure, the experimental evidence remains elusive and controversial. This calls for a careful examination of the relation between the band dispersion predicted by ground state DFT and the ARPES intensity maps that are recorded in experiment. Moreover, the polarization dependence of ARPES can be utilized for highlighting different bands, and for revealing their elemental and orbital character. The orbital character of the surface bands is important for technological applications, since it determines the sensitivity of the electronic structure of the system against controlled and uncontrolled chemical reactions at the surface.

Here we report a detailed study of the surface band structure of MoTe<sub>2</sub>(T<sub>d</sub>) by means of DFT calculations. To the best of our knowledge, we present the first ARPES calculations for this system using a one-step model description. We analyze the orbital character of the near-Fermi level bands and predict a strong polarization dependence of the ARPES spectra. The calculated ARPES intensity maps are in good agreement with new, high-resolution experimental data obtained with a LASER source. The results show how specific bands and atomic species can be highlighted in ARPES with appropriate polarization, providing valuable guidelines for future ARPES measurements.

The rest of the paper is organized as follows. In Section II the computational and experimental methods are outlined. In Sec. III, the results of the ground state band structure and of the ARPES calculations are presented. The polarization dependence of the ARPES spectra is studied in detail and analyzed in terms of the orbital character of the bands. Then, the theoretical ARPES maps are compared with experiment. Finally, in Sec. IV we summarize and conclude our work.

## II. THEORETICAL AND EXPERIMENTAL METHODS

Two types of calculations are performed. First, the ground state band structure at the MoTe<sub>2</sub>(T<sub>d</sub>) surface is computed with DFT in a repeated slab geometry. Second, ARPES simulations are performed using the one-step model of photoemission. Throughout this paper, the experimental structure with lattice constants  $a = 3.477 \text{ \AA}$ ,  $b = 6.335 \text{ \AA}$ ,  $c = 13.883 \text{ \AA}$  [21] is used. The crystal structure is shown in Fig. 1. Surface relaxation has been checked with DFT and found negligible, as expected for layered materials with weak van-der-Waals forces between layers such as MoTe<sub>2</sub>.

### A. Ground state band structure calculations

The surface is modeled using a slab of four  $\text{MoTe}_2$  layers and over 10 Å vacuum spacing between slabs, resulting in a supercell lattice parameter  $c = 37.8$  Å. The projector-augmented wave method as implemented in the Vienna *ab initio* simulation package (VASP) [24] is used with the commonly adopted [14] Perdew-Burke-Ernzerhof (PBE) exchange-correlation functional [25]. The calculations are performed on a  $16 \times 10 \times 1$   $\mathbf{k}$ -points mesh in the Brillouin zone and the plane-wave basis energy cut-off is set to 400 eV. The spin-orbit interaction (SOI) is taken into account in all calculations.

### B. One-step ARPES calculations

The ARPES calculations are done with the spin-polarized relativistic Korringa-Kohn-Rostoker (SPR-KKR) package [26]. As in the slab calculations, the experimental crystal structure and the PBE exchange-correlation potential are used. The SOI is treated exactly through the Dirac equation. The Atomic Sphere Approximation (ASA) is used and the KKR equations are solved with an angular momentum cut-off of  $l_{max} = 3$ . After computing the bulk Green's function, a surface model is constructed and the Green's function of the semi-infinite surface is found by solving a Dyson equation. We perform one-step model ARPES calculations [26–29] for the semi-infinite surface model using the Layered Korringa-Kohn-Rostoker (LKKR) multiple scattering theory [29–32].

As the crystal structure of  $\text{MoTe}_2$  is not densely packed but contains a large interstitial volume, empty spheres must be added when using the ASA to obtain converged, self-consistent potentials. As a result, SPR-KKR yields a ground state band structure in excellent agreement with the VASP calculations. However, we found that the empty spheres inside a  $\text{MoTe}_2$  layers lead to numerical difficulties in the LKKR calculations, needed for ARPES. This is related to the fact that in LKKR, compact 2D scattering layers must be defined. In  $\text{MoTe}_2$  the crystal planes are rumpled which may lead to complications when solving the multiple scattering equations between layers [31, 32]. Therefore, in the ARPES calculations, we have removed the empty spheres inside the  $\text{MoTe}_2$  layers and kept only those between the layers, see Fig. 1 a. The same strategy has already been applied successfully to another TMDC material ( $\text{WTe}_2$ , Ref. [13, 33]). As a result, the ARPES band dispersions of  $\text{MoTe}_2$  agree well with the DFT-VASP bands as seen in Fig. 2.

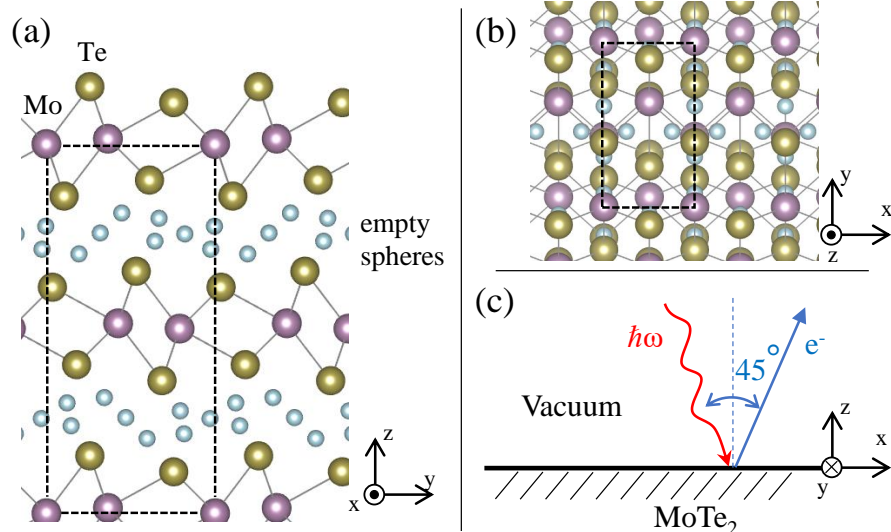


FIG. 1. (a,b) Ball and stick model of  $\text{MoTe}_2$  surface. Dotted lines indicate unit cell. Mo in purple, Te in yellow, empty spheres in light blue. (a) Side view. (b) Top view. (c) Experimental geometry.

### C. Experimental details

The 1T'- $\text{MoTe}_2$  sample, grown by a chemical vapor transport method, was cleaved inside the ultra-high vacuum chamber using the scotch-tape method under a pressure below  $8 \times 10^{-9}$  Pa. A shiny mirror-like surface, indicating the

high quality of the sample, was obtained after cleaving. High-resolution ARPES measurements were performed at the  $\mu$ -ARPES system of Hiroshima Synchrotron Radiation Center (HiSOR), Japan [34]. Photoelectrons, which were excited by a vacuum-ultraviolet laser ( $\hbar\omega = 6.27$  eV), were collected by a hemispherical photoelectron analyzer (VG Scienta R4000). The light was incident in the  $xz$ -plane, making an angle of  $45^\circ$  with the electron emission direction (Fig. 1 c). The energy and spatial resolutions were better than 3 meV and  $5\mu\text{m}$ , and the angular resolution was less than  $0.05^\circ$ . During the ARPES measurement, the sample was maintained at a temperature of 67 K, well below the  $1\text{T}'$  to  $T_d$  transition point.

### III. RESULTS AND DISCUSSIONS

#### A. Band structure of $\text{MoTe}_2(T_d)$

In  $\text{MoTe}_2(T_d)$ , topologically non-trivial bands have been predicted near the  $\bar{\Gamma} - \bar{X}$  line ( $k_y = 0$ ) of the Brillouin zone between the hole pocket centered at  $k_x = 0$  and the electron pocket around  $k_x = 0.3 \text{ \AA}^{-1}$  [14]. Here we focus on this region in  $(\mathbf{k}, E)$  space. The DFT band structure obtained with the slab model is shown in Fig. 2 along with ARPES simulations for unpolarized light, obtained by summing over x-, y- and z-linear polarization. Here, we have chosen a photon energy of 60 eV as used in the experiments of Ref. [17]. The band dispersion in the ARPES map agrees well with the VASP-DFT band structure, which shows that the ASA used in the KKR calculations provides an accurate representation of the crystal potential of  $\text{MoTe}_2$ . The band structure in Fig. 2 is in good agreement with other calculations [14] and features an electron and a hole pocket along  $k_x$ , as well as a flat surface state.

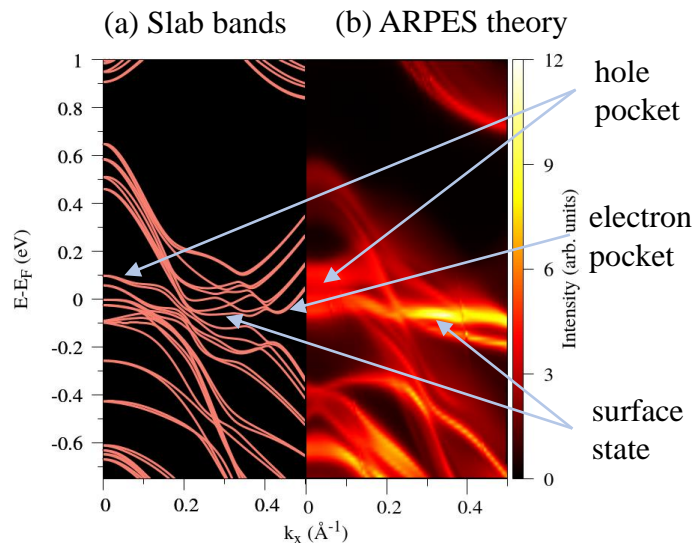


FIG. 2. Theoretical  $\text{MoTe}_2$  band structure along  $\bar{\Gamma} - \bar{X}$  of the 2D Brillouin zone. (a) Ground state slab model calculations. (b) ARPES calculations for unpolarized light and a photon energy of 60 eV.

#### B. Orbital projected bands and ARPES polarization dependence

Here we analyze the orbital character of the bands near the Fermi level and the relation to the ARPES polarization dependence. In the one-step ARPES calculations, final state and matrix element effects are fully taken into account and the predicted polarization dependence should be a reliable guide for experiments. In addition, a semi-quantitative model of the polarization dependence based on the valence band structure alone is very useful and can be gained by considering optical selection rules. The  $\text{MoTe}_2$  valence band near  $E_F$  is dominated by Mo 4d and Te 5p orbitals as seen in Fig. S1 of the Supplemental Material. We limit our analysis to these two orbitals. The photoemission intensity is proportional to the square of the transition matrix element

$$M_{if} = \langle \phi_f | \hat{e} \cdot \mathbf{r} | \phi_i \rangle, \quad (1)$$

where  $|\phi_i\rangle$ ,  $|\phi_f\rangle$ ,  $\hat{e}$  and  $\mathbf{r}$  are initial and final state wave function, light polarization vector and electron position operator, respectively. According to the dipole selection rules, an electron can transit from an initial state with angular momentum  $l$  to a final state of angular momentum  $l \pm 1$ . In the following, we discuss only  $l \rightarrow l-1$  transitions for simplicity. The  $l \rightarrow l+1$  transitions, which often dominate at high energy, give rise to a more complex, but generally less pronounced polarization dependence. To see this, consider e.g. a  $p_z$  initial state. The  $l \rightarrow l-1$  transition leads to an  $s$ -wave final state and a strong  $\cos^2 \theta$  polarization dependence, where  $\theta$  is the angle between the electric field vector and the  $z$ -axis. In particular, the intensity is zero for  $x$ - and  $y$ -linearly polarized light. In contrast,  $l \rightarrow l+1$  transitions from  $p_z$  to one of the five  $d$ -orbitals are possible for any light polarization such that the intensity never vanishes.

In the  $l \rightarrow l-1$  channel considered here, only the following transitions are possible from Mo  $d$  and Te  $p$  initial states for linear polarized light. X-polarization: Te  $p_x \rightarrow s$ , Mo  $d_{xz} \rightarrow p_z$ . Y-polarization: Te  $p_y \rightarrow s$ , Mo  $d_{yz} \rightarrow p_z$  and Mo  $d_{xy} \rightarrow p_x$ . Z-polarization: Te  $p_z \rightarrow s$  and Mo  $d_{z^2} \rightarrow p_z$ . Other transitions are forbidden by the dipole selection rules. From these considerations, we expect that ARPES with x-polarized light will reveal the bands with a large Te  $p_x$  and Mo  $d_{xy}$  orbital character. The calculated ARPES spectra for 60 eV light and x-polarization are compared with the DFT bands projected onto Te  $p_x$  and Mo  $d_{xz}$  orbitals in Fig. 3. Here and in all following DFT band plots, projection is done on the surface Te atoms and the subsurface Mo atoms. The Mo intensity is divided by a factor of two in order to roughly account for the ARPES surface sensitivity. Note that this Mo:Te weight ratio also corresponds to bulk MoTe<sub>2</sub>. Most ARPES features can be well identified with either of the two initial states. DFT bands projected on other Te or Mo orbitals resemble much less the ARPES map, as can be seen in Figs. S2 and S3 of the Supplemental Material. This indicates that the orbital character of the bands together with the  $l \rightarrow l-1$  dipole selection rules provides a qualitative understanding of the polarization dependence of the ARPES spectra. In Fig. 3 b,c, the strongest intensity appears around  $k_x = 0 \text{ \AA}^{-1}$  ( $= \bar{\Gamma}$  in 2D Brillouin Zone) for both Te  $p_x$  and Mo  $d_{xz}$  initial states. The ARPES for x-polarization is most intense around  $k_x = 0 \text{ \AA}^{-1}$  just below the Fermi level, which can be attributed to the Te  $p_x$  orbital. In addition, other high intensity ARPES bands correspond to the hole pocket. As seen from Fig. 3 they are mainly due to Mo  $d_{xz}$  character. Small energy shifts exist between the KKR-computed ARPES bands and the VASP-DFT bands. This is expected because of the different approximations used in the two approaches, most importantly the atomic sphere approximation in KKR. With this in mind, the most intense Mo  $d_{xz}$  bands (at  $E \sim -0.7 \text{ eV}$ ,  $k_x \sim 0$ ) also agree well with the ARPES bands. From the foregoing analysis, we conclude that linear polarization along the x-axis is a good choice for observing the hole pocket in MoTe<sub>2</sub>. In experiment, this corresponds to  $s$ -polarization with light incidence in the  $yz$  plane.

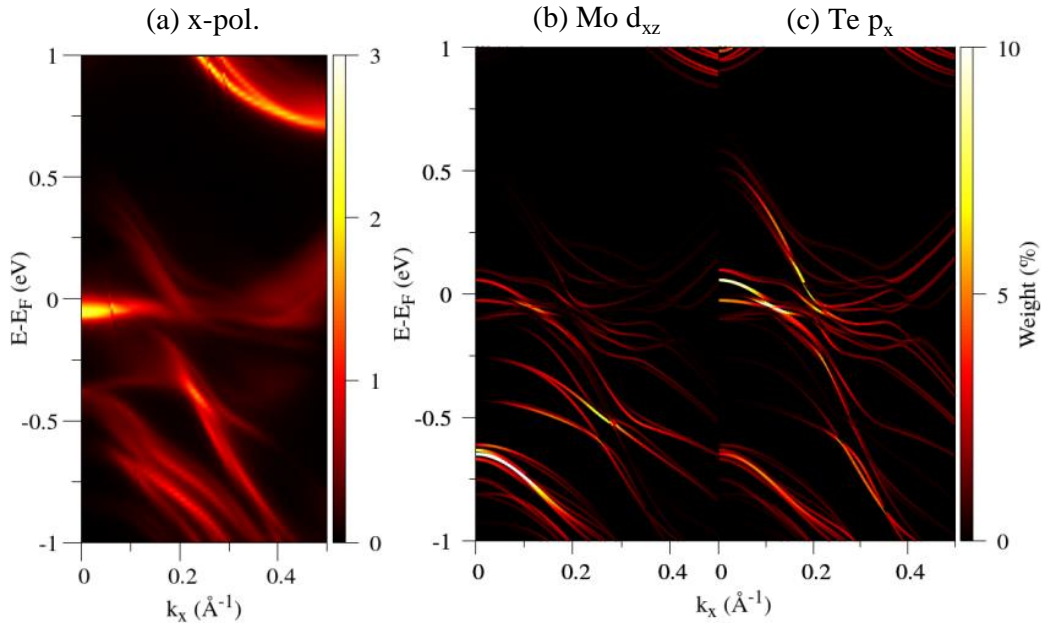


FIG. 3. (a) Calculated ARPES map for x-polarized light ( $\hbar\omega = 60$  eV). Note the strong intensity at the hole pocket. (b,c) DFT bands projected on the Mo  $d_{xz}$  (b) and Te  $p_x$  orbital (c).

The calculated ARPES spectra for  $y$ -polarization and the corresponding projected bands are shown in Fig. 4. In the case of  $y$ -polarization,  $l \rightarrow l-1$  transitions are possible only from Mo  $d_{xy}$ , Mo  $d_{yz}$  and Te  $p_y$  initial states. In the Mo  $d_{xy}$  and Mo  $d_{yz}$  projection, the dominant feature is a group of bands which disperses linearly from  $k_x = 0 \text{ \AA}^{-1}$ ,  $E = 0.5 \text{ eV}$  to  $k_x = 0.4 \text{ \AA}^{-1}$ ,  $E = -1 \text{ eV}$ . Closer inspection shows that they are made of two groups of bands, where the upper part joins the electron pocket at  $k_x \approx 0.3 \text{ \AA}^{-1}$ . The lower part evolves into the hole pocket around the  $\bar{\Gamma}$  point. These linearly dispersing bands are clearly seen as a bright feature in the calculated ARPES spectra. The projection on the Te  $p_z$  bands shows moderately intense bands in the region  $k_x < 0.3 \text{ \AA}^{-1}$ ,  $E < -0.7 \text{ eV}$  which can explain the corresponding bands seen in the ARPES plot. However, the Te  $p_y$  contribution is very weak for all bands above  $-0.4 \text{ eV}$ , and so the Te  $p_y$  orbital plays no role for the electron and hole pockets.

For both  $x$ - and  $y$ -polarized light, the calculated ARPES intensity is very weak compared to  $z$ -polarization (see Fig. 5 below). This is because the considered  $k$ -range around the  $\bar{\Gamma}$  point of the Brillouin zone corresponds to near normal emission, i.e. an emission direction perpendicular to the photon electric field vector in the  $xy$ -plane. It is well known that perpendicular emission is generally much weaker than parallel emission [35]. In the popular plane wave approximation, perpendicular emission is even impossible [22]. Yet, the existence of some pronounced ARPES features at  $\mathbf{k} = 0$  for both  $x$ - and  $y$ -polarized light shows that the plane wave approximation can be misleading [36, 37] and that one-step model calculations are needed for a correct interpretation of ARPES spectra.

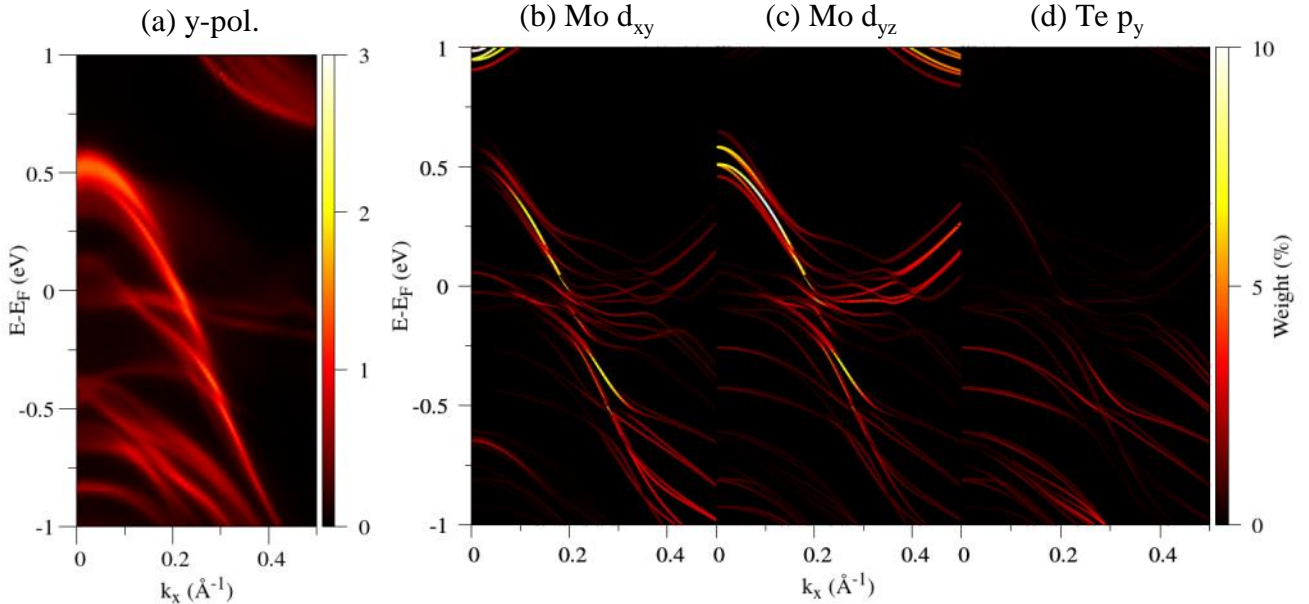


FIG. 4. (a) Calculated ARPES intensity for  $y$ -polarized light ( $\hbar\omega = 60 \text{ eV}$ ). A group of strong ARPES bands form a linearly dispersing line. (b-d) DFT bands projected on the Mo  $d_{xy}$  (b), Mo  $d_{yz}$  (c) and Te  $p_y$  orbital (c).

In Fig. 5 the calculated ARPES spectra for  $z$ -polarization are shown along with possible orbital projected DFT bands, namely Mo  $d_{z^2}$  and Te  $p_z$ . The Mo  $d_{z^2}$ -projection shows strong intensity for a group of bands which form an arc-like structure around  $E = -0.8 \text{ eV}$  which agrees well with the most intense features of the ARPES map. Concerning the Te  $p_z$  projected bands, large intensity is seen for a flat band around the electron pocket, which has been identified as a surface state [14, 15]. This corresponds to a bright flat line in the ARPES map at  $k_x > 0.25 \text{ \AA}^{-1}$ ,  $E \approx -0.1 \text{ eV}$ . By comparison with Figs. 3,4 it is clear that electron pocket and surface state can be best visualized with  $z$ -polarized light. This is in agreement with the experiments by Crepaldi et al. [15] who observed the surface state with strong intensity with mixed  $s$ - and  $p$ -polarized light (containing some  $z$ -polarization) while the surface state intensity almost vanished for pure  $s$ -polarized light (which contains zero  $z$ -polarization). In  $z$ -polarization, the electric field vector of the photon field is nearly parallel to the emission direction. This explains why the overall ARPES intensity is much larger than for in-plane ( $x$  or  $y$ ) polarization. Experimentally, exact  $z$ -polarization is impossible but can be approached by using  $p$ -polarization and grazing incidence.

The foregoing analysis shows that the ARPES polarization dependence can qualitatively be understood from the orbital-projected DFT bands and the dipole selection rules. It is clear however, that such an initial state theory cannot give a quantitative description of ARPES intensity maps. Indeed, final state effects play an important role too, and are responsible for the photon energy dependence. Note that the present one-step-model calculations include

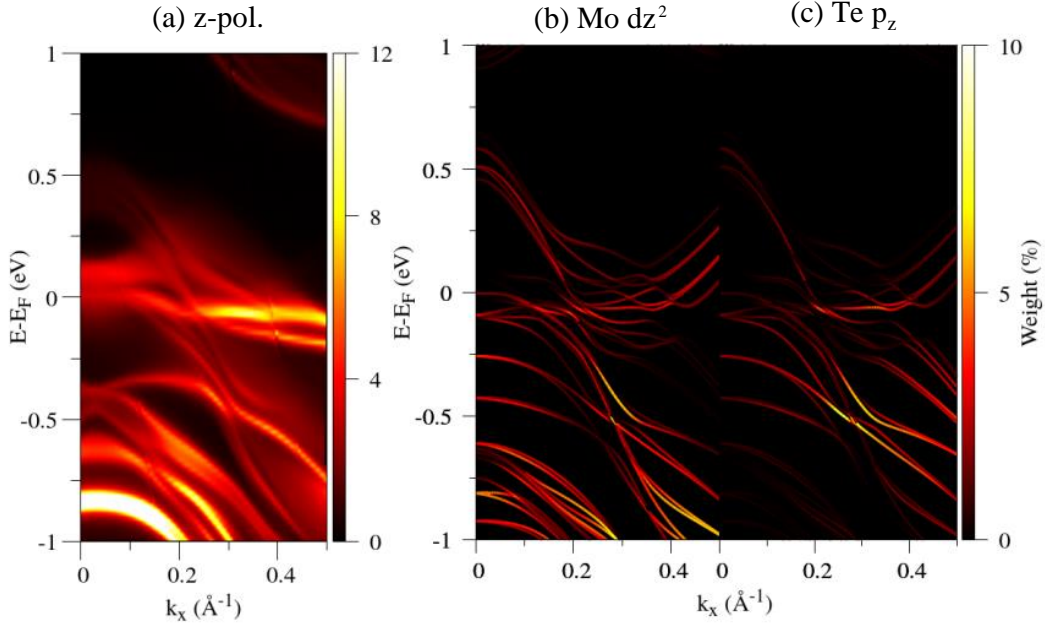


FIG. 5. (a) Calculated ARPES intensity for z-polarized light ( $\hbar\omega = 60$  eV). Note that the color scale is enhanced by a factor of 4 as compared to Figs. 3 and 4. (b,c) DFT bands projected on the Mo  $d_{z^2}$  (b) and Te  $p_z$  orbital (c).

all matrix and final state effects.

Despite its qualitative nature, the orbital-projected bands and selection rule analysis, are very useful for determining what polarization is best suited for probing particular parts of the band structure and for understanding the nature of the bonding. In the case of MoTe<sub>2</sub>, we have seen that the electron pocket and the surface state can be observed with z-polarization, whereby the Te  $p_z$  contribution is highlighted. X-polarization reveals the Te  $p_x$  bands and is a good choice for observing the hole pocket. With  $y$ -polarization, mainly Mo  $d_{xy}$  and  $d_{yz}$  orbitals are probed which form a group of linear dispersing bands which join either the electron or the hole pocket.

### C. Comparison with experiment

Tamai et al. [17] measured the MoTe<sub>2</sub> ARPES along  $k_x$  with 60 eV light and  $p$ -polarization, corresponding to a combination of  $x$ - and  $z$ -polarized light. Both electron and hole pocket were observed with high intensity. In contrast,  $s$ -polarization suppresses the electron pocket and the surface state intensity as observed by Crepaldi et al. [15]. Both experimental results can be explained by our polarization analysis.

Here we have measured the ARPES of MoTe<sub>2</sub> near the Fermi energy along the  $\bar{\Gamma}-\bar{X}$  line ( $k_x < 0.4 \text{ \AA}^{-1}$ ) using a photon energy of 6.27 eV and  $s$ -polarized light (polarization vector along the  $y$ -axis). See Fig. 1 c for the experimental geometry. The experimental data is shown in Fig. 6, along with the corresponding one-step ARPES calculation. Both the measured and the calculated ARPES map are dominated by a group of strongly dispersing bands, marked 2-4 in Fig. 6 a. As seen from the comparison with the projected bands (Fig. 6, d-f) these features are mainly of Mo  $d_{xy}$  and Mo  $d_{yz}$  character. Feature 4 may be assigned to the hole pocket while features 1-3 belong to lower energy bands with similar dispersion. Features 5 and 6 are part of the electron pocket, where the intense band 5, is dominated by Mo  $d_{xy}$  and  $d_{yz}$  orbitals, while the weak feature 6 is essentially of Mo  $d_{yz}$  character. Experiment and theory disagree somewhat about the  $k_x$ -positions of the various features. The calculated feature 2 is shifted by  $0.1 \text{ \AA}^{-1}$  to higher  $k_x$  with respect to experiment, which could be due to limitations of the surface barrier model used in the KKR calculations. Furthermore, the splitting between hole and electron pocket is smaller in the calculation than in experiment (features 4 and 5). Apart from these details, the calculated ARPES intensity map agrees very well with the data. Both in experiment and theory, the electron and hole pockets appear as nearly touching, tilted cones, as depicted in Fig. 6 c. This finding hints to a Weyl semi-metallic character of MoTe<sub>2</sub>.

The ARPES calculations in Fig. 4 a and Fig. 6 b were obtained with the same light polarization but different

photon energies, 60 and 6.27 eV, respectively. When comparing the same binding energy range, we find that the two ARPES intensity maps are very similar, except that with 6.27 eV photons, the average intensity is over one order of magnitude larger than with 60 eV photons. We conclude that for the bands in the vicinity of the electron and hole pocket studied here, the light polarization has a much more pronounced effect on the ARPES map than the photon energy, which mainly changes the average intensity.

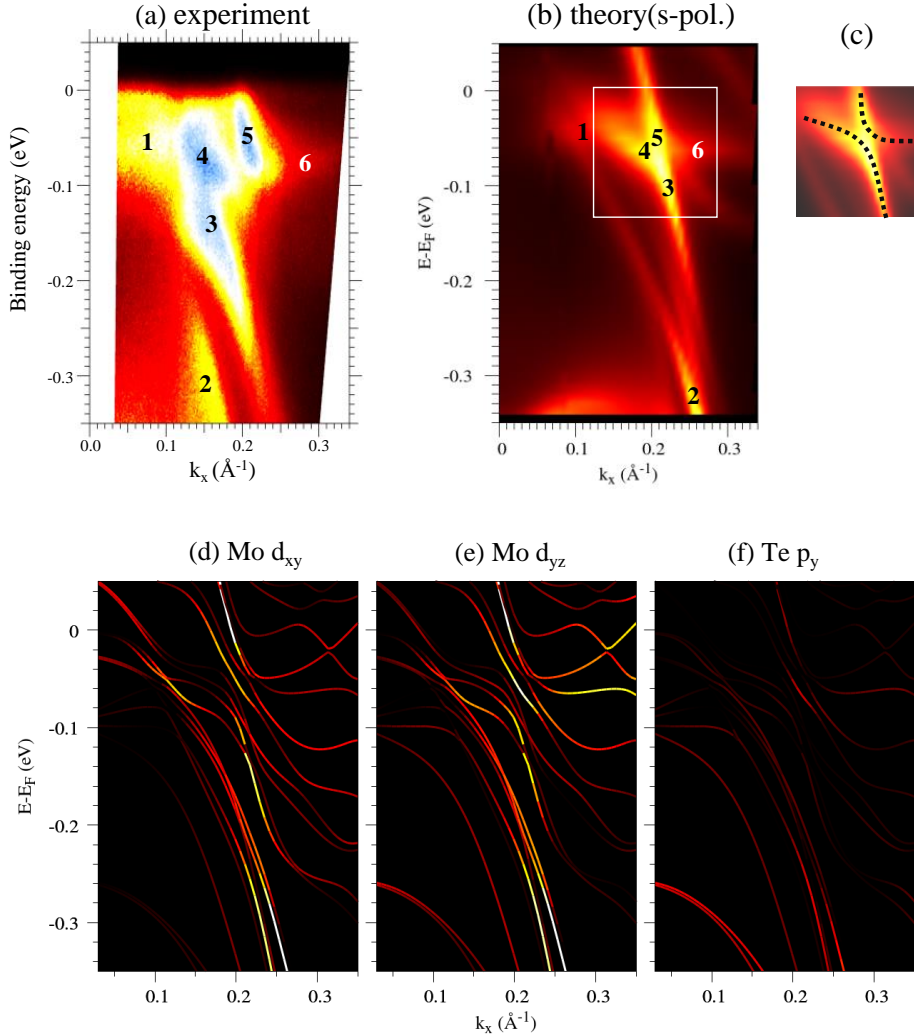


FIG. 6. Comparison between experimental (a) and theoretical (b) ARPES intensity maps for  $\hbar\omega = 6.27$  eV and s-polarized light. (c) Detail of (b) highlighting the electron and hole pockets forming tilted cones. (d-e) Corresponding orbital projected bands. This is the same data as in Fig. 4 plotted on an enlarged  $E$ -scale for easy comparison with (a,b).

#### IV. CONCLUSIONS

In summary, we have presented a combined experimental and theoretical study of the band structure of the Weyl semi-metal candidate material  $\text{MoTe}_2(\text{T}_d)$ . The orbital character of the near Fermi-energy bands has been analyzed using density functional theory. We find that along the  $\bar{\Gamma} - \bar{X}$  line, the hole pocket is dominated by the Te  $p_x$  orbital, while the electron pocket is mainly made of Mo  $d_{yz}$  and Te  $p_z$  derived bands. We have performed one-step-model ARPES calculations and obtained good agreement with the experimental data. The ARPES intensity depends strongly on the light polarization, which can be understood from the orbital character of the bands together with the dipole selection rules. The results show how relevant parts of the near Fermi-energy band structure, especially electron-pocket, hole-pocket and surface state, can be highlighted using the most suitable light polarization. More

generally, we conclude that one-step-model ARPES calculations are indispensable for a quantitative interpretation of ARPES data with complex band structures typical for topological 2D materials.

## V. ACKNOWLEDGMENTS

We are very grateful to Prof. Keiji Ueno of Saitama University for providing us the MoTe<sub>2</sub> sample. R.O. thanks financial support by the NIM Summer Research Program of the University of Munich (LMU) and by the Frontier Science Program of Chiba University. J.S. and J.M. would like to thank CEDAMNF project financed by the Ministry of Education, Youth and Sports of Czech Republic, Project No. CZ.02.1.01/0.0/0.0/15\_003/0000358. J.B. and H.E. acknowledge financial support by the DFG via the projects Eb 158/32 and Eb 158/36.

- 
- [1] S. Y. Xu, I. Belopolski, N. Alidoust, M. Neupane, G. Bian, C. Zhang, R. Sankar, G. Chang, Z. Yuan, C. C. Lee, S. M. Huang, H. Zheng, J. Ma, D. S. Sanchez, B. K. Wang, A. Bansil, F. Chou, P. P. Shibayev, H. Lin, S. Jia, and M. Z. Hasan, *Science* **349**, 613 (2015).
- [2] V. Aji, *Phys. Rev. B* **85**, 241101(R) (2012).
- [3] A. A. Zyuzin and A. A. Burkov, *Phys. Rev. B* **86**, 115133 (2012).
- [4] D. T. Son and B. Z. Spivak, *Phys. Rev. B* **88**, 104412 (2013).
- [5] A. Burkov, *Annual Review of Condensed Matter Physics* **9**, 359 (2018).
- [6] H. B. Nielsen and M. Ninomiya, *Phys. Lett. B* **130**, 389 (1983).
- [7] H. Weng, C. Fang, Z. Fang, B. A. Bernevig, and X. Dai, *Phys. Rev. X* **5**, 011029 (2015).
- [8] B. Q. Lv, H. M. Weng, B. B. Fu, X. P. Wang, H. Miao, J. Ma, P. Richard, X. C. Huang, L. X. Zhao, G. F. Chen, Z. Fang, X. Dai, T. Qian, and H. Ding, *Phys. Rev. X* **5**, 031013 (2015).
- [9] S.-M. Huang, S.-Y. Xu, I. Belopolski, C.-C. Lee, G. Chang, B. Wang, N. Alidoust, G. Bian, M. Neupane, C. Zhang, S. Jia, A. Bansil, H. Lin, and M. Z. Hasan, *Nature Communications* **6**, 7373 (2015).
- [10] A. A. Soluyanov, D. Gresch, Z. Wang, Q. Wu, M. Troyer, X. Dai, and B. A. Bernevig, *Nature* **527**, 495 (2015).
- [11] Z. Wang, D. Gresch, A. A. Soluyanov, W. Xie, S. Kushwaha, X. Dai, M. Troyer, R. J. Cava, and B. A. Bernevig, *Phys. Rev. Lett.* **117**, 056805 (2016).
- [12] T.-R. Chang, S.-Y. Xu, G. Chang, C.-C. Lee, S.-M. Huang, B. Wang, G. Bian, H. Zheng, D. S. Sanchez, I. Belopolski, N. Alidoust, M. Neupane, A. Bansil, H.-T. Jeng, H. Lin, and M. Zahid Hasan, *Nature Communications* **7**, 10639 (2016).
- [13] M. Fanciulli, J. Schusser, M. Lee, Z. E. Youbi, O. Heckmann, M. C. Richter, C. Cacho, C. Spezzani, D. Bresteau, J.-F. Hergott, P. D’Oliveira, O. Tcherbakoff, T. Ruchon, J. Minár, and K. Hricovini, *Phys. Rev. Research* **2**, 013261 (2020).
- [14] Y. Sun, S.-C. Wu, M. N. Ali, C. Felser, and B. Yan, *Phys. Rev. B* **92**, 161107(R) (2015).
- [15] A. Crepaldi, G. Autès, A. Sterzi, G. Manzoni, M. Zucchigna, F. Cilento, I. Voborník, J. Fujii, P. Bugnon, A. Magrez, H. Berger, F. Parmigiani, O. V. Yazyev, and M. Grioni, *Phys. Rev. B* **95**, 041408(R) (2017).
- [16] J. Jiang, Z. K. Liu, Y. Sun, H. F. Yang, C. R. Rajamathi, Y. P. Qi, L. X. Yang, C. Chen, H. Peng, C.-C. Hwang, S. Z. Sun, S.-K. Mo, I. Voborník, J. Fujii, S. S. P. Parkin, C. Felser, B. H. Yan, and Y. L. Chen, *Nature Communications* **8**, 13973 (2017).
- [17] A. Tamai, Q. S. Wu, I. Cucchi, F. Y. Bruno, S. Riccò, T. K. Kim, M. Hoesch, C. Barreteau, E. Giannini, C. Besnard, A. A. Soluyanov, and F. Baumberger, *Phys. Rev. X* **6**, 31021 (2016).
- [18] B. E. Brown, *Acta Crystallogr.* **20**, 268 (1966).
- [19] H. P. Hughes and R. H. Friend, *Journal of Physics C: Solid State Physics* **11**, L103 (1978).
- [20] T. Zandt, H. Dwelk, C. Janowitz, and R. Manzke, *Journal of Alloys and Compounds* **442**, 216 (2007).
- [21] Y. Qi, P. G. Naumov, M. N. Ali, C. R. Rajamathi, W. Schnelle, O. Barkalov, M. Hanfland, S.-C. Wu, C. Shekhar, Y. Sun, V. Süß, M. Schmidt, U. Schwarz, E. Pippel, P. Werner, R. Hillebrand, T. Förster, E. Kampert, S. Parkin, R. J. Cava, C. Felser, B. Yan, and S. A. Medvedev, *Nature Communications* **7**, 11038 (2016).
- [22] P. Puschnig, S. Berkebile, A. J. Fleming, G. Koller, K. Emtsev, T. Seyller, J. D. Riley, C. Ambrosch-Draxl, F. P. Netzer, and M. G. Ramsey, *Science* **326**, 702 (2009).
- [23] C. Datzer, A. Zumbülte, J. Braun, T. Förster, A. B. Schmidt, J. Mi, B. Iversen, P. Hofmann, J. Minár, H. Ebert, P. Krüger, M. Röhlfsing, and M. Donath, *Phys. Rev. B* **95**, 115401 (2017).
- [24] G. Kresse and J. Furthmüller, *Phys. Rev. B* **54**, 11169 (1996).
- [25] J. P. Perdew, K. Burke, and M. Ernzerhof, *Phys. Rev. Lett.* **77**, 3865 (1996).
- [26] H. Ebert, D. Ködderitzsch, and J. Minár, *Rep. on Prog. in Phys.* **74**, 096501 (2011).
- [27] J. Braun, H. Ebert, and J. Minár, in *Spintron. from Electron. to devices*, edited by C. Felser and G. H. Fecher (Springer, 2013) pp. 97–114.
- [28] J. Minár, J. Braun, S. Mankovsky, and H. Ebert, *Journal of Electron Spectroscopy and Related Phenomena* **184**, 91 (2011).
- [29] J. Braun, J. Minár, and H. Ebert, *Physics Reports* **740**, 1 (2018).
- [30] J. Braun, *Rep. on Prog. in Phys.* **59**, 1267 (1996).
- [31] F. Máca and M. Scheffler, *Computer Physics Communications* **51**, 381 (1988).

- [32] K. Kambe, A KKR method for two-dimensional lattices and its application to band calculation, in *Computational Methods in Band Theory: Proceedings of a Conference held at the IBM Thomas J. Watson Research Center, Yorktown Heights, New York, May 14–15, 1970, under the joint sponsorship of IBM and the American Physical Society*, edited by P. M. Marcus, J. F. Janak, and A. R. Williams (Springer US, Boston, MA, 1971) pp. 409–415.
- [33] J. Schusser, L. Nicolaï, M. Fanciulli, M. I. Lee, Z. E. Youbi, O. Heckmann, C. Richter, K. Hricovini, and J. Minár, AIP Conf. Proc. **2131**, 20041 (2019).
- [34] H. Iwasawa, E. F. Schwier, M. Arita, A. Ino, H. Namatame, M. Taniguchi, Y. Aiura, and K. Shimada, Ultramicroscopy **182**, 85 (2017).
- [35] S. Goldberg, C. Fadley, and S. Kono, Journal of Electron Spectroscopy and Related Phenomena **21**, 285 (1981).
- [36] A. M. Bradshaw and D. P. Woodruff, New Journal of Physics **17**, 013033 (2015).
- [37] P. Krüger, Journal of the Physical Society of Japan **87**, 061007 (2018).